Journal of Alloys and Compounds 1041 (2025) 183867

Contents lists available at ScienceDirect

Journal of Alloys and Compounds

journal homepage: www.elsevier.com/locate/jalcom

A cellular automata-based crystal plasticity analysis of slip activity in additive manufactured Ti-6Al-4V during dwell fatigue

Hanqing Liu [a], Masanori Kitamura [a], Fabien Briffod [b], Takayuki Shiraiwa [a,*]

[a] Department of Materials Engineering, The University of Tokyo, 7-3-1 Hongo, Bunkyo-ku, Tokyo 113-8656, Japan
[b] Research Center for Structural Materials, National Institute of Materials Science, 1-2-1 Sengen, Tsukuba, Ibaraki 305-0047, Japan

ARTICLE INFO

Keywords:
Ti-6Al-4V
Additive manufacture
Dwell fatigue
Cellular Automaton
Crystal plasticity Finite element method
Slip

ABSTRACT

A numerical approach combining cellular automaton and crystal plasticity finite element methods was proposed to investigate slip behaviors of additive manufactured Ti-6Al-4V material under dwell fatigue condition. Compared with conventional polygon-based microstructure models, the proposed method generates microstructures that more closely resemble the actual material and allows the simulation to explicitly account for the influence of grain shapes on local stress distributions and slip system activation. A Burgers orientation relationship based minimum elastic strain energy indicator was introduced to determine the α-variant selection during the β-to-α phase transformation. A cellular automata code, ExaCA tool was utilized to generate a selective laser melting fabricated microstructure. The crystal plasticity parameters of the model were calibrated based on tensile test results of the additive manufactured specimen and subsequently applied to the dwell fatigue simulation. The results reveal material hardening arising from accumulated slip system activations and show the relationship between load shedding and slip activity, which is consistent with our previous findings. This approach overcomes the limitations of traditional modeling methods and offers the potential to elucidate the underlying fatigue mechanisms of additively manufactured Ti-6Al-4V alloys.

1. Introduction

Driven by increasing demands for lightweight design and energy efficiency, selective laser melting (SLM) has been widely used in fields of aerospace, automobiles, and space technology [1,2]. As an additive manufacturing (AM) technique, SLM enables the fabrication of metal parts with high strength and complex internal and external structure. In SLM process, the product is constructed with a powder bed fusion technique, where a high-energy concentrated laser selectively melts metal powder on a building platform, following pre-designed scanning strategy [3]. In addition to offering greater design freedom for part geometries, SLM can also reduce both lead time and cost when compared to traditional manufacturing methods [4].

SLM-manufactured components are often subjected to extreme and complex cyclic loading conditions [5], which imposes specific requirements on the metal alloys used. Ti-6Al-4V is a commonly used material in SLM, particularly in aerospace applications where dwell fatigue is a critical concern due to its excellent corrosion resistance and high strength [6–8]. Furthermore, the SLM-produced Ti-6Al-4V parts demonstrate a comparable fatigue performance as the traditional rolled alloy [9]. Typically, Ti-6Al-4V alloy can exhibit an equiaxed microstructure, in which both α grains and β grains exhibit irregular polygon shapes, as well as a bimodal microstructure consisting of equiaxed primary α grains and transformed β areas [10,11]. In SLM process, the build strategy and laser parameters employed significantly influence the microstructure of as-built specimens, which in turn leads to considerable variations in their mechanical performance [12]. Additionally, SLM-manufactured materials are prone to inevitable defects, such as lack of fusion, high thermal stress gradients, inferior surface quality, and process-induced porosity [13,14], all of which can substantially reduce their serving lives. Therefore, investigating the mechanical properties and failure mechanisms of SLM- fabricated Ti-6Al-4V components in dwell fatigue is an urgent and essential task.

Nowadays, various methodologies are employed to study SLM-processed Ti-6Al-4V alloys, which can generally be categorized into two approaches: experimental investigation and numerical simulation. Gaur et al. [13] experimentally studied the cyclic plasticity behavior and the cold dwell sensitivity of SLM-processed Ti-6Al-4V alloy, and found out a significant reduction in the fatigue lives of specimens exposed to a dwell period at relatively lower strain amplitudes. Nevertheless, it

* Corresponding author.
E-mail address: shiraiwa@rme.mm.t.u-tokyo.ac.jp (T. Shiraiwa).

https://doi.org/10.1016/j.jallcom.2025.183867
Received 9 July 2025; Received in revised form 17 September 2025; Accepted 17 September 2025
Available online 18 September 2025

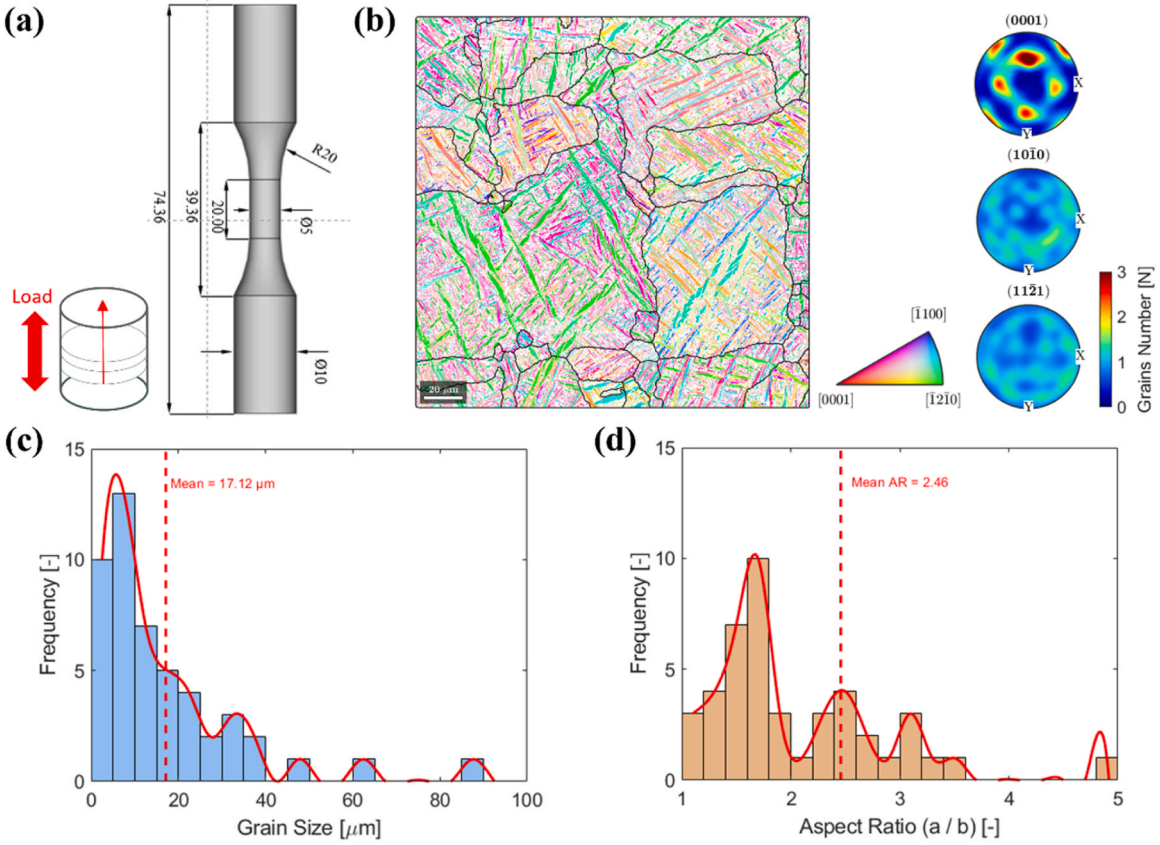

Fig. 1. SLM-built Ti-6Al-4V specimen. (a) building direction, load direction and specimen dimensions; (b) inverse pole figure map and pole figures of α phase; (b) prior β grain size distribution; (c) prior β grain aspect ratio distribution.

remains challenging to gain a fundamental understanding of the local deformation behavior solely through experimental approaches. To overcome this limitation, Hu et al. [15] combined the practical experiment with a high-resolution digital image correlation (HR-DIC) analysis method to investigate the slip system activities in primary α grains of a forged Ti–6Al–4 V alloy under pure fatigue and dwell-fatigue conditions. While the slip activity associated with dwell fatigue was successfully verified, the process incurred significant expenditures of time and financial resources. To address the challenges associated with experimental verification, various numerical approaches have been proposed. Cai et al. [16] established a simplified polycrystalline representative volume element (RVE) model to study the effect of microstructure and defect on fatigue behavior in dual-phase Ti-6Al-4V. However, their model was based on polygonal geometries resembling a honeycomb structure, which significantly deviates from the actual microstructure of SLM-fabricated Ti-6Al-4V materials. Moreover, the generated grains were limited to simple polygonal shapes, making it impossible to realistically capture the grain size distribution and morphological features observed in practice. Similarly, Bridier et al. [17] developed a honeycomb-like structure in which the grains were simplified into hexagonal prisms to investigate the slip activity in Ti–6Al–4 V under high-cycle fatigue loading, while completely neglecting the influence of grain morphological characteristics. Developing microstructures that more closely resemble the actual conditions through AM process simulations has become a new research focus. Chen et al. [18] used a cellular automaton (CA) method to generate more complex and realistic microstructures. For the phase transformation, although they employed the Burgers orientation relationship (BOR), which demonstrates that each β grain can produce twelve α variants, their study did not provide a theoretical basis for determining which α variants actually form.

Furthermore, in studies on the dwell fatigue behavior of Ti-6Al-4V alloys, the phenomenon of load shedding [15,19,20] has been frequently reported. Load shedding refers to the redistribution of stress from a soft grain to its neighboring harder grains during the dwell period, while the underlying mechanisms remain poorly understood due to the lack of grain-level stress resolution in experiments. Numerous studies have investigated the use of numerical simulation methods to examine the fatigue behavior of AM-fabricated Ti-6Al-4V. However, most of these works have overlooked the distinctive microstructural features arising from the AM process compared to conventionally manufactured materials. In addition, the β-to-α phase transformation based on the BOR still lacks a reliable methodology.

In order to overcome the problem of model distortion and the insufficient reliability in describing the β-to-α phase transformation in SLM-fabricated Ti-6Al-4V, as well as investigating the loading shedding phenomenon, this study proposes an integrated CA and crystal plasticity finite element (CPFE) framework, along with a BOR-based minimum elastic strain energy indicator for α-variant selection. A microstructural model was constructed by simulating the SLM process and nucleation mechanism using CA method and subsequently simplified based on the BOR. The crystal plasticity (CP) parameters of the obtained model were calibrated with experimental tensile test results. Finally, the influence of grain orientation on slip system activity during dwell fatigue was explored with the CPFE simulations.

2. Experimental methods

2.1. Material

Specimens used in this study were fabricated by AconityMINI (Aconity 3D) machine with a laser power of 120 W, a scan speed of 1000 mm/s, a scan pitch of 80 μm, a layer thickness of 30 μm, and a spot

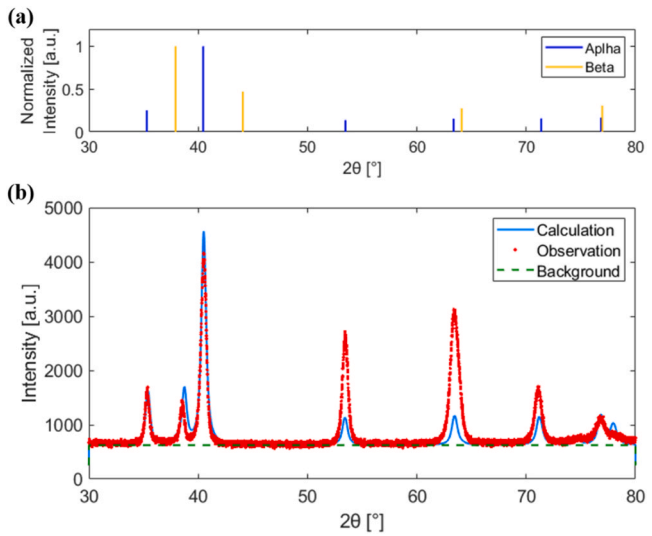

Fig. 2. XRD results of the SLM-fabricated Ti-6Al-4V specimen: (a) normalized X-ray diffraction patterns of α phase and β phase in Ti-6Al-4V; (b) observed and calculated XRD patterns, along with the background noise.

diameter of 80 μm, under an argon atmosphere [21]. The Ti-6Al-4V alloy powder used was a commercial product from Osaka Titanium Technologies Co., Ltd. The specimens were built along the horizontal direction, and their dimensions are shown in Fig. 1(a). The inverse pole figure (IPF) map and pole figures of α phase, obtaining from the electron backscatter diffraction (EBSD), are shown in Fig. 1(b), and a lamellar-like α/β microstructure can be observed. EBSD was conducted over a 200 μm × 200 μm area. By counting the pixels of the α phase and β phase, it is calculated that the volume fraction of the α phase reaches as high as 99.17 %. The prior β grains were reconstructed using the open-source MATLAB toolbox MTEX. The black outlines in EBSD represent the grain boundaries of the reconstructed prior β grains. Grains with an area smaller than 9 μm^2 were excluded from subsequent analysis to eliminate potential artifacts and improve data reliability. The material is an alloy with an average grain diameter ($d = 2\sqrt{Area/\pi}$) of 17.2 μm and a mean aspect ratio of 2.4 within prior β grains, as shown in Fig. 1(c) and (d), indicating the presence of numerous elongated grains. It is worth noting that coarse grains with a grain diameter approaching 90 μm were identified in the microstructure. According to the pole figures of (0001), $(10\bar{1}0)$, $(11\bar{2}1)$ directions, the specimen exhibits a relatively weak texture around (0001) direction along the AM building direction, with four intensity peaks approximately equal to a value of 3.

To further validate the volume fraction of the different phases in SLM-fabricated Ti-6Al-4V specimen, XRD was performed, and the results are presented in Fig. 2. The normalized X-ray diffraction patterns of α phase and β phase in Ti-6Al-4V are shown in Fig. 2(a), where distinct distributions of characteristic peaks can be identified. Fig. 2(b) presents both the experimentally observed and the calculated XRD patterns, along with the background noise. A strong correspondence between the diffraction peaks of the α phase and the experimental data indicates a dominant presence of the α phase in the specimen. To quantitatively determine the phase fractions, the XRD patterns were refined using the Rietveld method implemented in the open-source GSAS software. To achieve a high level of consistency with the experimental results, the volume fraction of the α phase was calculated to be in the range of 98.2–100 %, which confirms the feasibility of calculating the α-phase volume fraction through the pixel distribution in EBSD.

2.2. Tensile test procedure

The tensile test was conducted using a Shimadzu AG-X plus testing machine under strain-controlled conditions with a strain rate of 0.001 s^{-1} at room temperature. Strain was measured using an extensometer and two strain gauges attached to both ends of the specimen to ensure accurate displacement monitoring. The test was terminated when the specimen completely fractured into two segments.

3. Numerical methods

The workflow of the CA and CPFE methods involved in this study is illustrated in Fig. 3. The grain morphology features obtained from EBSD were used to validate the CA results. Due to the characteristics of ExaCA,

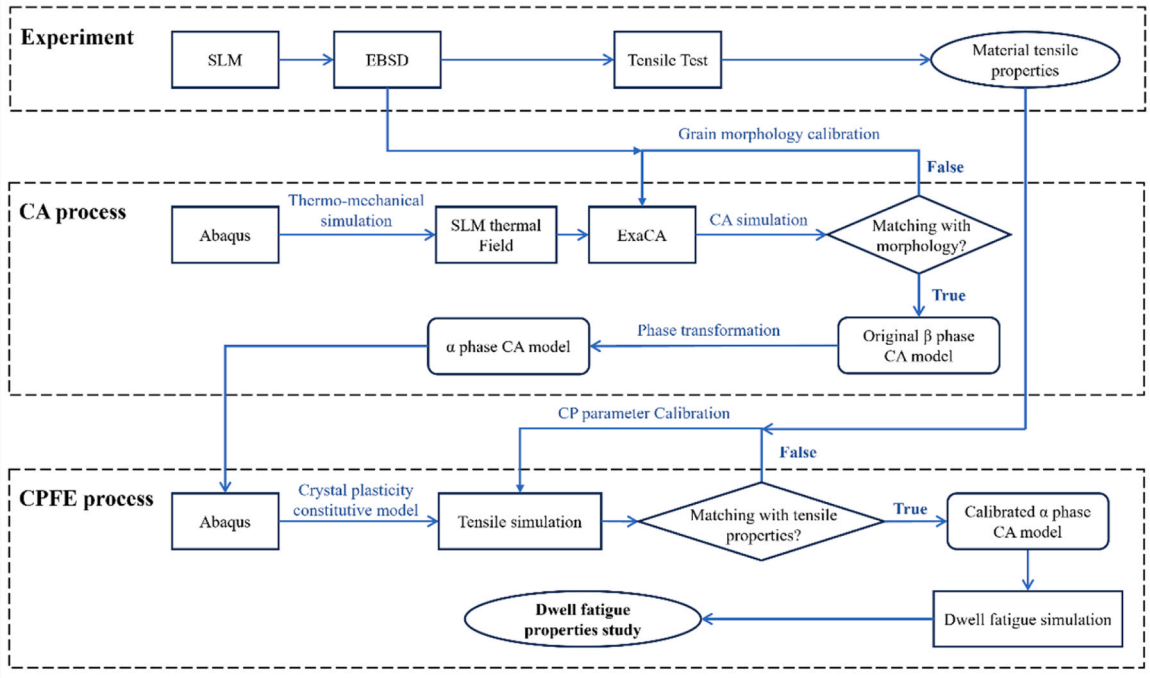

Fig. 3. Schematic figure of the CA and CPFE simulations.

Table 1
Material constants for Ti-6Al-4V in CA process.

conductivity (W/(m·K)))	density (kg/m^3)	specific Heat (J/(kg·K))
7.5	4430	520

Table 2
SLM parameters in CA process.

laser power (W)	scan speed (mm/s)	scan pitch (mm)	layer pitch (mm)	spot diameter (mm)	absorption efficiency
120	1000	0.08	0.03	0.08	0.5

the generated microstructure consists exclusively of the β phase with a BCC structure [22]. Once a crystal model with morphology similar to the reconstructed prior β grains in specimen was established, the β phase in the model was transformed into the α phase using the Burgers orientation relationship (BOR). This refined model was then applied to tensile simulations. By comparing the simulation results with tensile test data, the model parameters were optimized. Once a reasonable degree of agreement was achieved, the model was further employed to a dwell fatigue simulation, providing insights into the dwell fatigue characteristics of SLM-fabricated Ti-6Al-4V alloy. The detailed procedures of the CA and CPFE methods are presented in the following sections .

3.1. Cellular automaton procedure

The CA simulation was carried out by combining the ExaCA open-source software [22] and the FEM solver Abaqus. A Gaussian-distributed thermal field was employed to simulate the SLM process, implemented through a user-defined material subroutine (UMAT) in Abaqus with the laser scan path provided as input. Material constants for Ti-6Al-4V involved are shown in Table 1**.** In this process, a volumetric domain of 200 μm × 200 μm × 100 μm was discretized into a structured mesh consisting of 200 × 200 × 100 elements, resulting in a voxel size of 1 μm^3 , and was meshed using 8-node hexahedral elements (C3D8R). A fixed temperature of 298 K was imposed on the bottom surface of the domain to simulate thermal anchoring to a platform. A time-dependent surface heat flux was applied using a UMAT, which modeled a moving heat source that mimicked laser scanning. Subsequently, ExaCA tool was employed to simulate the grain growth process based on the obtained temperature field, thereby generating a relatively realistic and complex microstructure of Ti-6Al-4V. SLM parameters involved in CA process are shown in and Table 2. The nucleation density was set to 3 × 10^4 mm^{-3}, and 16 layers were computed.

3.2. Phase transformation method

At present, a widely employed strategy involves generating β phase models and subsequently transforming them into α phase configurations in accordance with the BOR [16–18,20]. In the present work, due to the fact that the α phase volume fraction of the SLM-fabricated Ti-6Al-4V material reaches 98.2 %, it is evident that the α phase plays a predominant role in governing the deformation behavior. Accordingly, the microstructure was simplified by treating the material as a fully α phase system.

In BCC/HCP alloy, the BOR is consistently maintained, which is typically defined as $(110)_\beta//(0001)_\alpha$ and $(\bar{1}11)_\beta//(\bar{2}110)_\alpha$ [23]. However, there are up to 12 distinct α-variants for a given β-orientations that can satisfy the BOR, which introduces significant complexity in the development of the model. To simplify the modeling process and ensure feasibility, for each β orientation, the α variant with the lowest interfacial energy was selected as the corresponding β phase [24,25].

The optimal α-variant orientation, denoted as ori_{HCP}, is determined by:

$$ori_{HCP} = ori_{BCC} \bullet \boldsymbol{V}^{(j)} \# \tag{1}$$

where the ori_{BCC} is the orientation of β phase in CA result, and $\boldsymbol{V}^{(j)}$ is the orientation transformation matrix of j-th variant based on BOR.

To identify the appropriate α-variant index j^*, an elastic strain energy indicator $E_{\text{int}}^{(j)}$ and a strain tensor indicator $\boldsymbol{\varepsilon}_{\text{int}}^{(j)}$ of j-th variant, associated with lattice misfit, are introduced as:

$$E_{\text{int}}^{(j)} = \text{tr}\left(\boldsymbol{\varepsilon}_{\text{int}}^{(j)T}\boldsymbol{\varepsilon}_{\text{int}}^{(j)}\right) \tag{2}$$

$$\boldsymbol{\varepsilon}_{\text{int}}^{(j)} = \frac{1}{2}(\boldsymbol{V}^{(j)T}\boldsymbol{V}^{(j)} - \boldsymbol{I}) \tag{3}$$

The optimal variant index j^* is then selected as the one minimizing the elastic strain energy indicator among all variants by:

$$j^* = \underset{j}{\text{argmin}} E_{\text{int}}^{(j)} \tag{4}$$

3.3. Crystal plasticity constitutive model

To better capture the effects of the microstructure of SLM-processed Ti-6Al-4V alloy on its deformation behavior, a crystal plasticity constitutive model is involved in CPFE method, achieved by applying user material subroutine through Abaqus [17,26].

In this model, the total deformation gradient F is given by:

$$\boldsymbol{F} = \boldsymbol{F}_e\boldsymbol{F}_p \tag{5}$$

where the $\boldsymbol{F}_e$ is the elastic gradient for lattice stretch and rigid body rotation, and $\boldsymbol{F}_p$ is the plastic gradient for dislocation slip.

The plastic velocity gradient $\boldsymbol{L}$ can be obtained through introducing elastic and plastic contributions of the velocity gradient, $\boldsymbol{L}_e$ and $\boldsymbol{L}_p$, respectively, and is expressed by:

$$\boldsymbol{L} = \dot{\boldsymbol{F}}\boldsymbol{F}^{-1} = \boldsymbol{L}_e + \boldsymbol{F}_e\boldsymbol{L}_p\boldsymbol{F}_e^{-1} \tag{6}$$

$$\boldsymbol{L}_p = \sum_i^{N_{slip}} \dot{\gamma}^{(i)}\left(\boldsymbol{s}^{(i)} \otimes \boldsymbol{n}^{(i)}\right) \tag{7}$$

where the N_{slip} is the number of slip systems considered in the model. The $\dot{\gamma}^{(i)}$, $\boldsymbol{s}^{(i)}$ and $\boldsymbol{n}^{(i)}$ are the shearing rate, slip plane direction and the slip plane normal for the i-th slip system, respectively. The shear rate $\dot{\gamma}^{(i)}$ can be calculated by:

$$\dot{\gamma}^{(i)} = \dot{\gamma}_0^{(i)}\left|\frac{\tau^{(i)}}{\tau_c^{(i)}}\right|^{n^s}\text{sgn}\left(\tau^{(i)}\right) \tag{8}$$

where the $\dot{\gamma}_0^{(i)}$ is a reference slip rate for the i-th slip system, n^s the strain rate exponent. $\tau^{(i)}$ is the resolved shear stress (RSS) for i-th slip system, which is related to the deformation and Cauchy stress tensor $\boldsymbol{\sigma}$, and are given by:

$$\tau^{(i)} = \boldsymbol{s}^{(i)} \otimes \boldsymbol{n}^{(i)} : \boldsymbol{\sigma} \tag{9}$$

The critical resolved shear stress (CRSS) $\tau_c^{(i)}$ for i-th slip system is contributed by three parts: the initial CRSS $\tau_0^{(i)}$, the Hall–Petch strengthening term and the hardening term:

$$\tau_c^{(i)} = \tau_0^{(i)} + \frac{k_{HP}}{\sqrt{d^{(i)}}} + \int_t \dot{\tau}_{S\to S}^{(i)}dt \tag{10}$$

Where k_{HP} is the Hall–Petch contribution coefficient, $d^{(i)}$ is the effective length scale for the slip system i, and $\dot{\tau}_{S\to S}^{(i)}$ the hardening rate due to slip-slip interactions. The value of $d^{(i)}$ was determined with lath thickness for

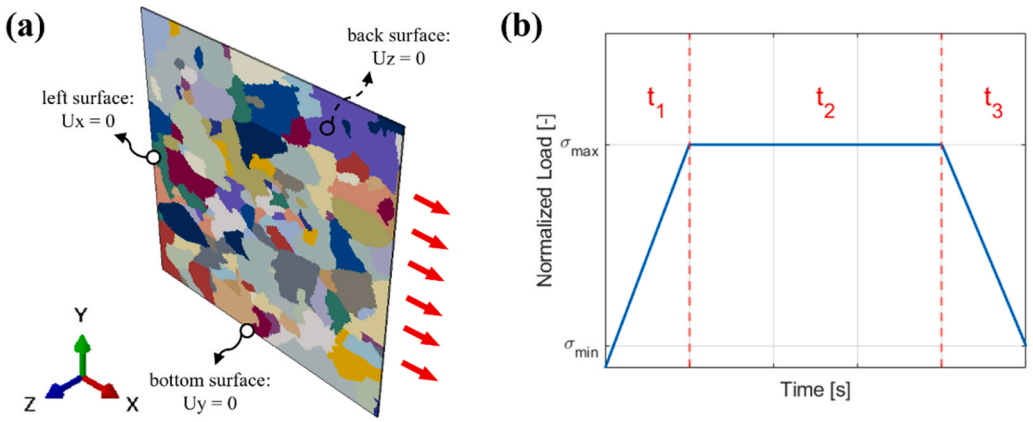

Fig. 4. The CP model obtained from CA process for tensile and dwell fatigue investigation. (a) Boundary conditions and load direction for both tensile and dwell fatigue simulation; (b) load condition for dwell fatigue simulation.

Table 3
Conditions for dwell fatigue simulation.

	maximum stress (MPa)	rise time (s)	dwell time (s)	fall time (s)
Sim 1	1022.2	2	120	2
Sim 2	992.2	2	120	2
Sim 3	1037.2	2	120	2
Sim 4	1052.2	2	120	2

two of the three prismatic slip systems, while the prior-β grain size was used for the remaining one [27,28].

The slip-slip hardening rate can be calculated by:

$$\dot{\tau}^{(i)}_{S\to S} = \frac{\tau^{(i)}_{S\to S}}{d\Gamma_S} \sum_{j=1}^{N_{slip}} h^{(i)(j)} \left| \dot{\gamma}^{(j)} \right| \tag{11}$$

$$\Gamma_S = \sum_{i=1}^{N_{slip}} \int_t \left| \dot{\gamma}^{(i)} \right| dt \tag{12}$$

where the Γ_S is the total accumulated shear strain, $h^{(i)(j)}$ is the slip-slip hardening coefficient between i-th and j-th slip systems. $\tau^{(i)}_{S\to S}$ is the slip-slip resistance and is defined by an extended Voce law:

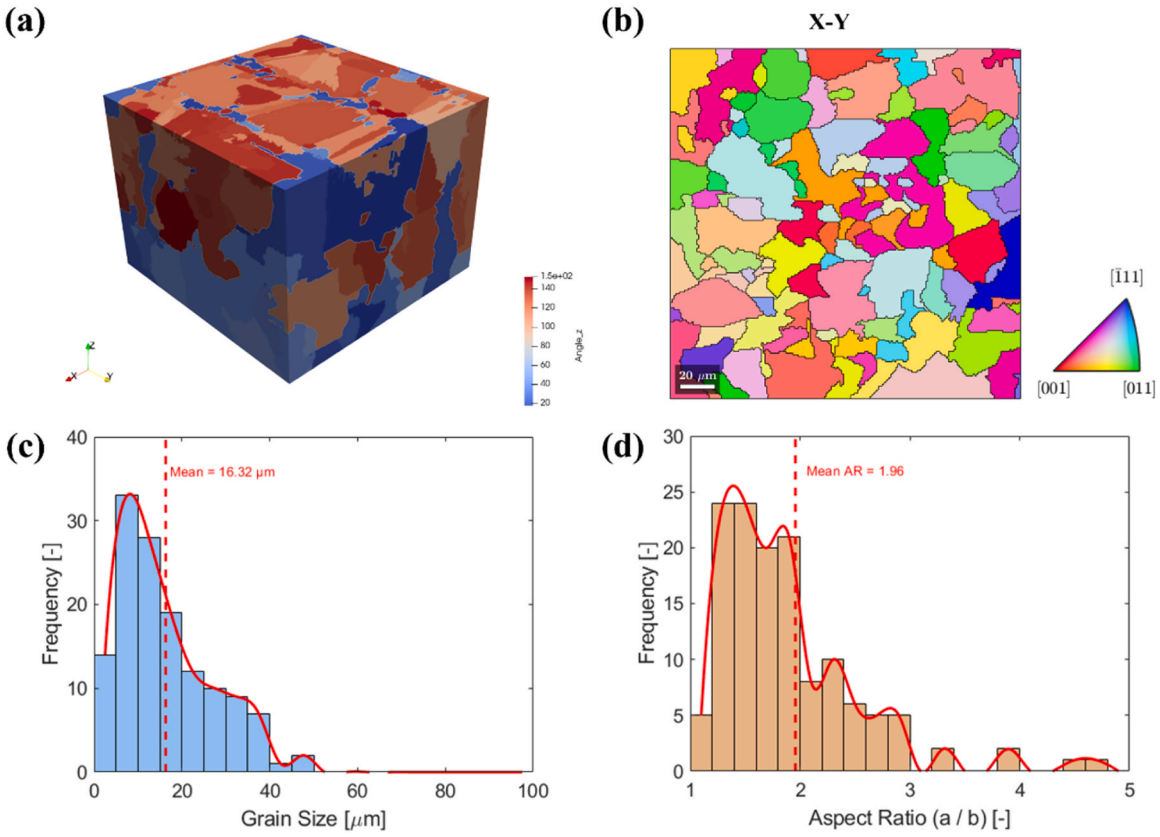

Fig. 5. Model obtained by ExaCA tool. (a) Three-dimensional model obtained by simulating the SLM process; (b) top surface β phase IPF; (c) grain size distribution of IPF; (d) grain aspect ratio distribution of IPF.

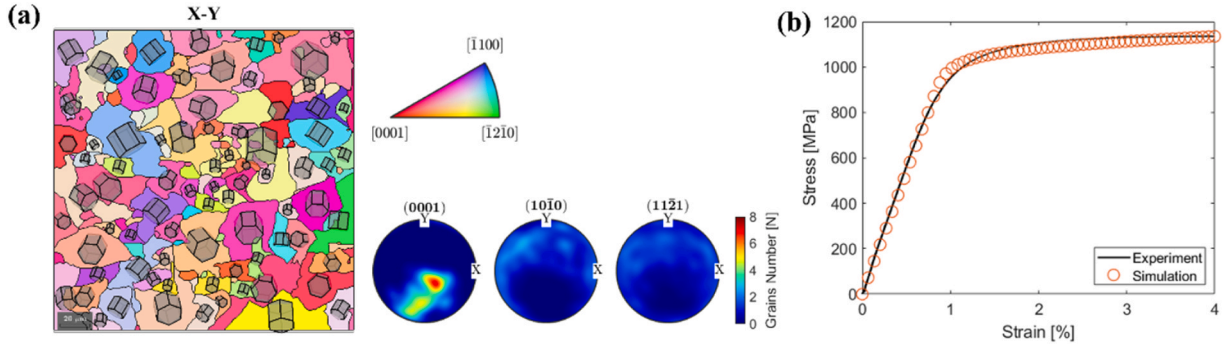

Fig. 6. (a) α-phase IPF and PF distribution obtained through BOR transformation; (b) Evaluation of tensile simulation results against experimental data.

$$\tau_{S\to S}^{(i)} = \left(\tau_1^{(i)} + h_1^{(i)}\Gamma_S\right)\left(1 - \exp\left(-\frac{b_1^{(i)}}{\tau_1^{(i)}}\Gamma_S\right)\right) \tag{13}$$

where the $\tau_1^{(i)}$, $b_1^{(i)}$ and $h_1^{(i)}$ are saturated CRSS, the initial hardening rate and asymptotic hardening rate for i-th slip system, respectively.

The parameters involved in the crystal plasticity constitutive model were calibrated based on the results of tensile tests on the SLM-fabricated Ti-6Al-4V specimen, which will be further elaborated in Section 4.

3.4. Numerical simulations

A 1 μm-thick slice was cut from the top of the CA model and converted into an Abaqus input file. The model with dimension of 200 μm × 200 μm× 1 μm contained 120 grains and was meshed with C3D8R. A voxel size of 1 μm^3 was applied to the model, leading to a total of 40,000 elements in the model. The material orientation properties of the model were assigned based on the calculated IPF distribution. To ensure the reliability of dwell fatigue simulation, the CP model was first calibrated with the tensile test results. The setup for tensile simulation is illustrated in Fig. 4(a), where three boundary conditions were applied to the model.

In the tensile simulation, the load was achieved by imposing a uniaxial strain along the x-axis with a constant strain rate of 0.001 s^{-1}, whereas in the dwell fatigue simulation, the load was applied through a periodic concentrated force.

Four sets of dwell fatigue simulations were conducted using the calibrated CP model derived from tensile simulation, and detailed conditions are shown in Table 3. These simulations were labeled as Sim 1 (S1), Sim 2 (S2), Sim 3 (S3) and Sim 4 (S4), respectively. The loading condition is shown in Fig. 4(b). The segment t_1 corresponds to the loading stage; the t_2 corresponds to the dwell stage; the t_3 corresponds to the unloading stage. A stress ratio of 0.1 was applied, and for time efficiency and feasibility, a total of 100 cycles were simulated. Generally, Ti-6Al-4V exhibits a relatively short fatigue life under high load conditions, especially when the applied stress exceeds the 0.2 % proof stress [15]. Performing 100 cycles provides sufficient information to investigate the longer-term dwell fatigue behavior [20]. Among these four simulations, S1 utilizes the 0.2 % proof stress obtained from the tensile calibration of the CP model as the applied dwell stress, with which the material exhibits a relatively short fatigue life and more pronounced slip activity [15]. Consequently, the subsequent discussion primarily focuses on the results from S1.

4. Results

4.1. Predicted microstructure with CA method

The model generated from CA process was constructed with dimensions of 200 μm × 200 μm× 190 μm as shown in Fig. 5(a). Since the laser passes only once at the top surface and does not represent the characteristic bulk microstructure, a 120 μm-high cross-section measured from the bottom surface in the vertical direction was extracted for analysis, as shown in Fig. 5(b). The β grain size distribution closely matches the EBSD results obtained from the experimental specimen in Section 2, with an average grain size of 16.3 μm. However, the CA procedure failed to simulate extremely large grains with size around 90 μm, as observed in the AM built specimen. This deviation is mainly attributed to the characteristics of ExaCA tool. Although the average grain size can be controlled by adjusting the nucleation density, the nucleation sites during grain formation are randomly assigned, making it difficult to generate grains with extreme large sizes. However, in our model, an influence factor based on grain size was incorporated into the activation of slip systems. Therefore, even in the absence of extreme large grains in the model, the reliability of the simulation results can still be ensured. Additionally, a slight deviation is noted in the grain aspect ratio distribution between the experimental data and the CA results, which may be attributed to the exclusion of extremely small grains with area less than 9 μm^2 during pre-processing of the EBSD data before analysis.

Table 4
CP parameters for Ti-6Al-4V alloys.

parameters		α phase
elastic stiffness (GPa)	C_{11}	162.4
	C_{12}	92.0
	C_{13}	69.0
	C_{33}	180.7
	C_{44}	46.7
CRSS (MPa)	τ_0^{basal}	465.0
	$\tau_0^{prismatic}$	409.7
	$\tau_0^{pyramidal<a>}$	542.7
	$\tau_0^{pyramidal<c+a>}$	653.3
saturated CRSS (MPa)	τ_1	τ_0 + 30.0
hardening parameters (MPa)	b_1	0
	h_1	425.0
Hall–Petch factor ($MPa\sqrt{mm}$)	k	17.3

4.2. Calibration of CP model

Since the α phase is not only significantly smaller than the prior β grains, but also exhibits an elongated shape and complex distribution, constructing an α/β dual-phase model for Ti-6Al-4V alloy is a highly challenging task. Additionally, up to six kinds of α variants were reported to form within a single prior β grain during martensitic transformation in solidification [27,29], which further increases the complexity of the microstructure. Consequently, most researchers simplified the α variants as parallel lathes, and their studies demonstrated that the simplified model is sufficient for predicting macroscopic stress–strain behavior while limitations remain for local-level analysis [16–18]. In this study, to ensure practical feasibility, the microstructure

Table 5
Tensile calibration evaluation.

	Experiment	CP simulation	Deviation	Percentage error
Young's modulus (GPa)	111.9	107.2	4.7	4.2 %
0.2 % proof stress (MPa)	978.0	1022.2	44.2	4.5 %
Yield strain	1.07 %	1.15 %	0.08 %	6.6 %

of SLM-fabricated Ti-6Al-4V material was simplified by neglecting the α phase structure, assuming each prior β grain was fully transformed into a single α variant. Following the phase transformation procedure outlined in Section 3, the entire microstructure generated by CA process was converted to the α variant with the lowest elastic strain energy indicator, as shown in Fig. 6(a). From corresponding the pole figures, a relatively strong (0001) texture with an intensity of approximately 8 can be found. This deviation from experimental results is attributed to the simplification introduced during the phase transformation procedure.

The CP parameters for Ti-6Al-4V model are listed in Table 4. Values of C_{11}, C_{12}, C_{13}, C_{33} and C_{44},along with the Hall–Petch factor, were obtained from referenced literatures [17,26]. These parameters primarily affect the stiffness properties of the model, and the results indicate that the model exhibits a good level of agreement in the elastic regime. However, since the CRSS value for different slip systems reported in previous studies often vary, only the CRSS ratios of each slip system were referenced from related work by other researchers [17] while adjustments on the values were made during the calibration process in this study, to ensure a satisfactory agreement in the plastic regime. The saturated CRSS for all slip systems were set to 30 MPa aligned with the calibration.

The calibration results are shown in Fig. 6(c) and Table 4. By comparing the experimental values and the simulated values, the reliability of the calibration was evaluated, as shown in Table 5. The results show deviations of 4.7 GPa in the Young's modulus, 44.2 MPa in the 0.2 % proof stress, and 0.08 % in the corresponding yield strain, among which, the largest percentage error is 6.6 %.

4.3. Dwell fatigue simulation

The stress-strain variations of all 100 cycles for four simulations are shown in Fig. 7(a), where obvious strain discrepancy can be observed. This indicates that the CP model exhibits high sensitivity to stress variations. Notably, the S4 terminated at the 6-th cycle due to non-convergent behavior caused by severe plastic deformation in Abaqus. The cumulated plastic strain of each cycle is plot in Fig. 7(b). In simulation S2, which applied a relatively lower load than the 0.2 % proof stress, minimal plastic strain was observed, likely due to the limited number of simulated dwell fatigue cycles. It is worth noting that under such loading conditions, the fatigue life of material is typically on the order of tens of thousands of cycles [30].

The strain variations of S1 during the dwell procedure in several fatigue cycles are shown in Fig. 8, where a significant change is observed in the early stages, followed by a stabilization of the stress as the number of fatigue cycles increases. Similar strain behaviors are also observed in other groups of simulations.

To elucidate the mechanism behind the observed stress variations, the distribution maps and iso-value of the maximum Schmid factor (SF) of each slip system family, including basal, prismatic, pyramidal<a> and pyramidal <c+a> slip systems, are plotted within the standard stereographic triangle, as presented in Fig. 9(a). Grain orientation plays a significant role in slip system activation. For the basal slip system, only a limited number of grains exhibit high SF values, whereas the other three slip systems show high SF values in most grains. This distinction is clearly illustrated in Fig. 9(b), where the basal system displays a relatively uniform SF distribution, while the SF values for the other slip systems are densely concentrated above 0.4.

Based on the characteristics of the SF distribution, three interconnected grains, highlighted by green dashed lines, were selected for detailed discussion in the subsequent sections, as shown in Fig. 10 (a). Grain 1 (G1) exhibits a misorientation angle of 90.2° between its (0001) plane and the loading direction. Grain 2 (G2) and Grain 3 (G3), which differ in orientation by only 0.3°, show misorientation angles of 57.4° and 57.3°, respectively, with respect to the loading direction. The misorientation angles between G1 and G2, and G1 and G3 are 81.6° and 81.9°, respectively.

Notably, the selected grains G1, G2, and G3 demonstrate

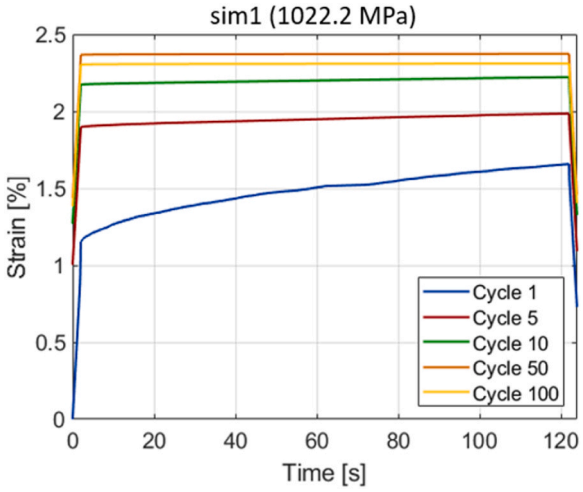

Fig. 8. Total strain variation across different fatigue cycles in S1.

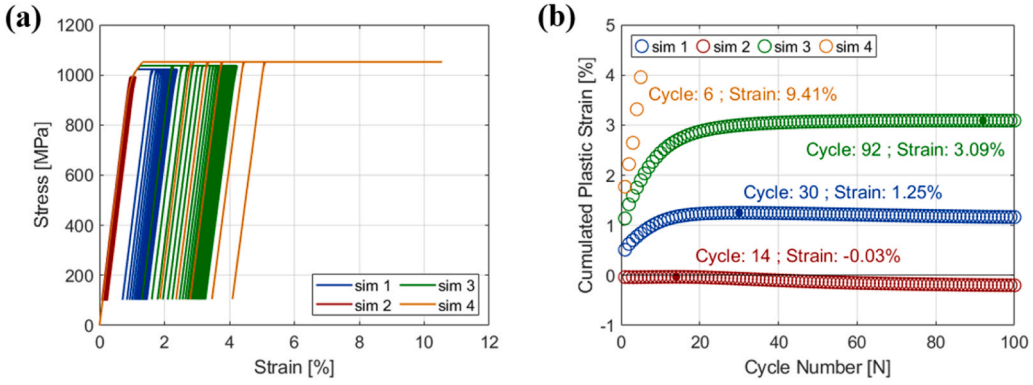

Fig. 7. Dwell fatigue simulation results of four groups of simulations. (a) Stress-strain curve; (b) cumulated plastic strain in each fatigue cycle.

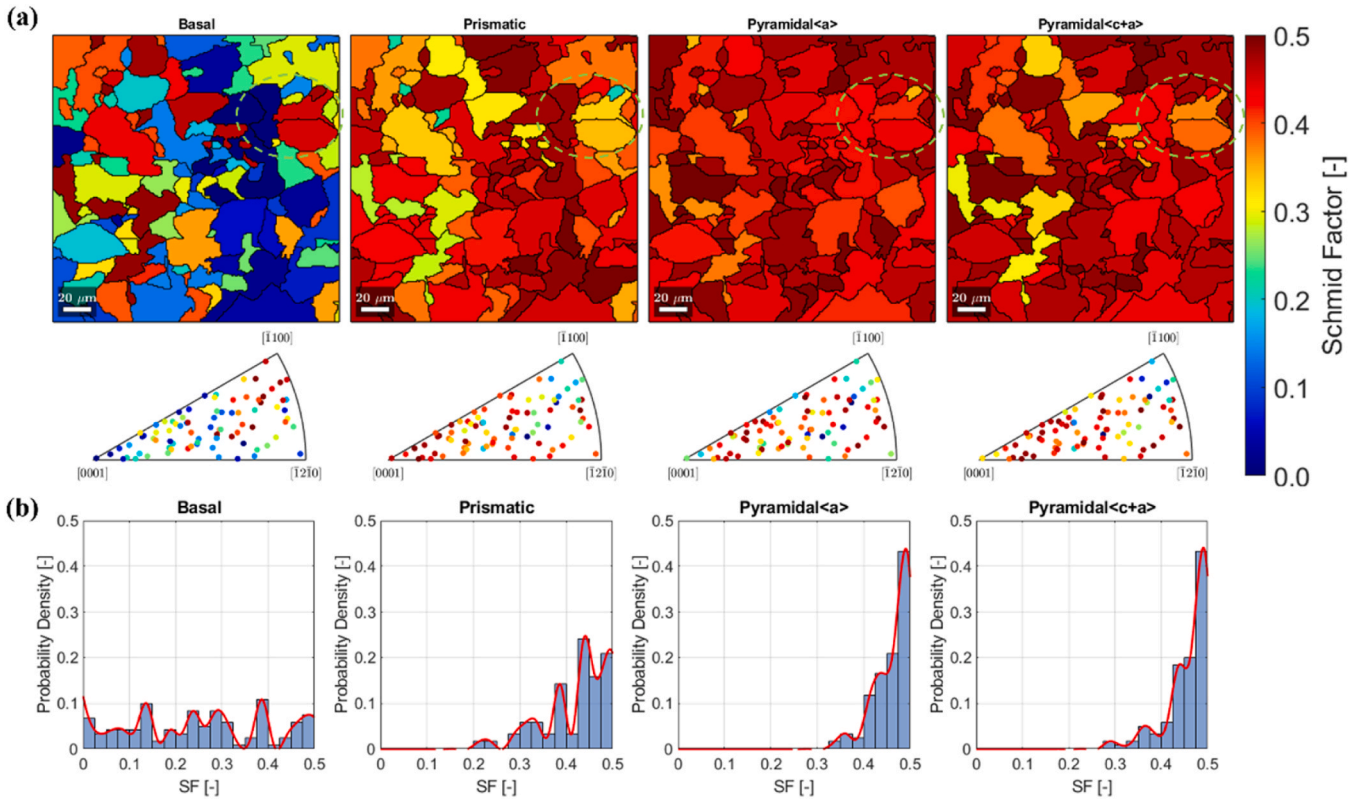

Fig. 9. Schmid factor distribution of four slip systems along the loading direction. (a) Distribution map and iso-values in the standard triangle; (b) probability density distribution.

considerable disparity in their SF distributions of basal slip system, while exhibiting similar distributions for the other slip systems. This indicates distinct slip activities within each grain. In general, the magnitude of the SF reflects the ease of slip activation; hence, G1 is classified as a hard grain, whereas G2 and G3 are regarded as soft grains. These distinct orientation relationships and SF distributions make G1, G2 and G3 ideal candidates for studying the influence of the grain orientations and load shedding phenomenon on dwell fatigue behaviors.

A path A-A' crossing the three grains was determined based on the stress distribution, and the variation of stress at dwell start (DS) and dwell end (DE) along the path is shown in Fig. 10 (b). The figure is divided into three regions by two grey vertical lines, which correspond to the two grain boundaries marked in Fig. 10 (a). Each region represents the part of the path within one of the three grains, respectively. It is evident that stress levels of both DS and DE increase with the number of fatigue cycles in G2 and G3. However, in G1, stress variation along the path exhibits a different trend.

The variation of stress change between the DS and DE along the path is shown in Fig. 10 (c). The maximum stress variation at the i-th cycle is calculated by:

$$\Delta\sigma^{(i)} = \sigma^{(i)}_{start} - \sigma^{(i)}_{end} \tag{14}$$

where the $\sigma^{(i)}_{start}$ and $\sigma^{(i)}_{end}$ are the stress at the beginning and end of dwell process, respectively.

In the early stages of dwell fatigue simulation, significant stress variations are observed along the path. As the number of cycles increases, these variations rapidly diminish and stabilize within approximately 10 cycles, showing strong consistency with the overall trend observed in Fig. 7(d). Additionally, a noticeable discontinuity in stress and stress variation can be observed at the grain boundary between G1 and G2. This is attributed to the nearly perpendicular orientation relationship between the two grains, which hinders the transmission of stress across the boundary. In contrast, no such discontinuity is observed between G2 and G3, further confirming the critical role of grain orientation in stress transmission.

Based on stress distribution along the path, three representative points, each located within one of the grains, were selected for further analysis on slip activities as highlighted in Fig. 10 (a). Point 1 (P1) locates in G1, point 2 (P2) locates in G2, and point 3 (P3) locates in G3. The stress variations during the dwell process in different fatigue cycles are shown in Fig. 11 (a), (b) and (c), respectively. Load shedding, as being reported in many literatures [15,20], is observed in P1 and P2. At P1, load shedding occurs only briefly during the initial fatigue cycles, while at P2, this phenomenon persists throughout the entire simulation. Moreover, the overall stress level at P1 decreases with increasing fatigue cycles, which contrasts with the trend observed at P2 and P3. At P3, an increasing stress trend is observed during the early stages of fatigue, exhibiting distinctly opposite stress variations compared to P2, despite both points being located in grains with nearly identical crystal orientations.

5. Discussion

5.1. Grain orientation and slip activity

While SF provides a preliminary indication of slip system activation likelihood, the CPFE framework enables direct extraction of the shear stress on each slip system. A comparison with the respective CRSS offers a more explicit and quantitative assessment of slip system activity. The shear stress for all slip systems involved in the S1 of CP model at P1, P2 and P3 are shown in Fig. 12 (a). In those figures, the shear stress variation of the 1st, 10th, 50th and 100th cycles are plotted together. In P1, only the prismatic slip system exhibits a shear stress greater than its corresponding CRSS, indicating its preferential activation before 50th load cycle. In both P2 and P3, only the basal slip system exhibits shear

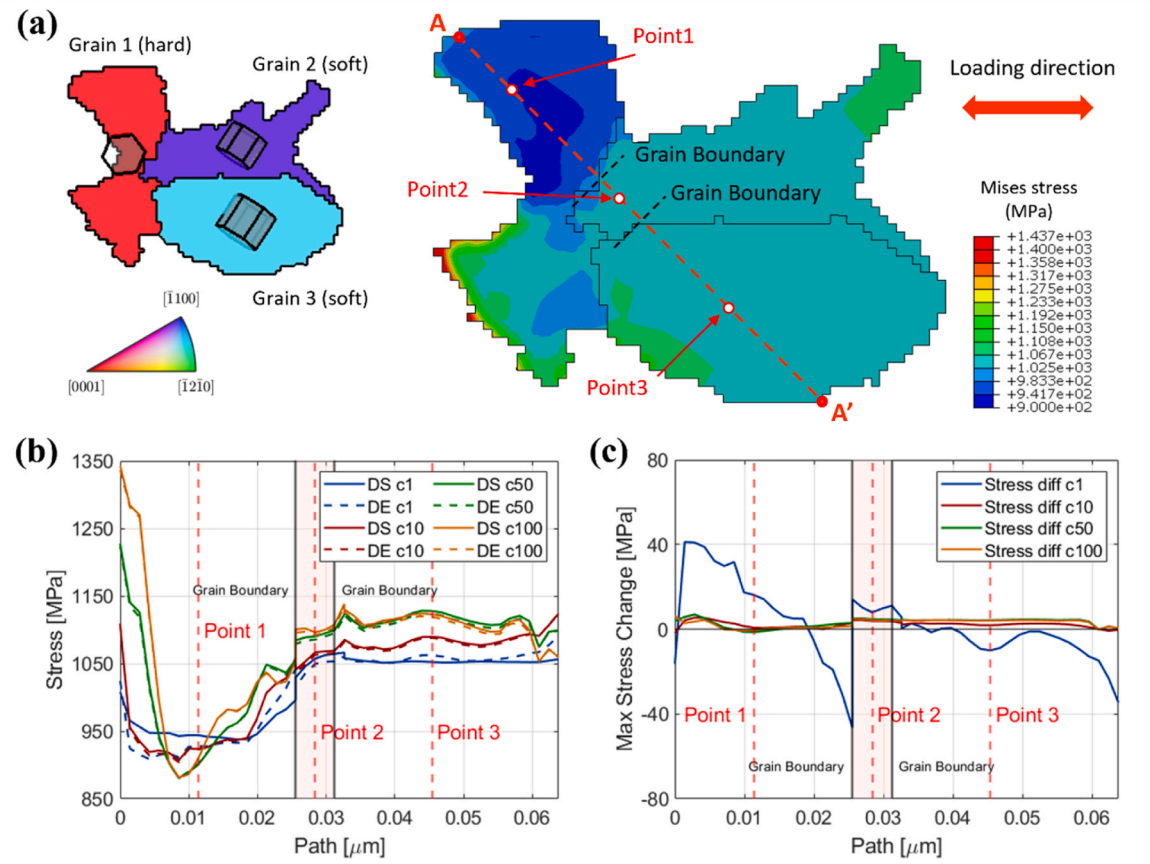

Fig. 10. Stress distribution of three soft-hard grains in Sim1. (a) Crystal orientations and stress distribution; (b) stress variations at the start and end of the dwell process in different fatigue cycles along the path A-A'. (c) maximum stress change of dwell process along the path A-A'.

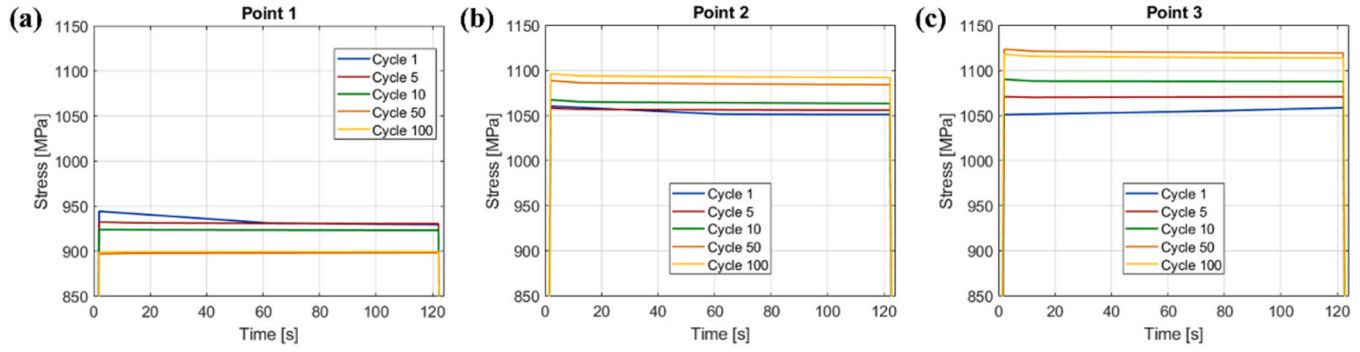

Fig. 11. The stress variation of different fatigue cycles in S1 at (a) point 1; (b) point 2; (c) point 3.

stress values exceeding the corresponding CRSS.

To better reveal the overall slip activities, the effective Schmid factors (ESF) of three points along with fatigue cycles are presented in the Fig. 13. The ESF $m_{eff}^{(i)}$ is calculated by:

$$m_{eff}^{(i)} = \frac{\tau_{RSS}^{(i)}}{\sigma_{app}} \tag{15}$$

where the $\tau_{RSS}^{(i)}$ is the shear stress of i-th slip system, and σ_{app} is applied macroscopic stress.

In P1, the ESF associated shows a decreasing trend as the number of fatigue cycles increases. These observations suggest that prismatic slip dominates the local plastic deformation in the early stages of dwell fatigue. However, as the number of cycles increases, the activation of the slip diminishes. In P2 and P3, the ESF for the basal slip remains relatively high throughout the simulation. These indicate that the basal slip system plays a dominant role in deformation behavior at these points during the entire dwell fatigue process.

To quantitatively analyze the behavior of activated slip systems in the three grains, rather than being limited to local points, the shear stress distributions of different slip systems for these grains are plotted in Fig. 14. Specifically, Fig. 14 (a) shows the shear stress distribution of prismatic slips for all pixels in grain G1. It can be seen that during cycles 1 to cycle 10, only a few regions exhibit shear stress exceeding the CRSS, indicating that only a small number of prismatic slips are activated. Afterward, the number of activated prismatic slips increases significantly. Furthermore, as the number of cycles increases, the shear stress in some regions exhibits a decreasing trend, while in other regions it shows an increasing trend. Clearly, P1 belongs to the former. This

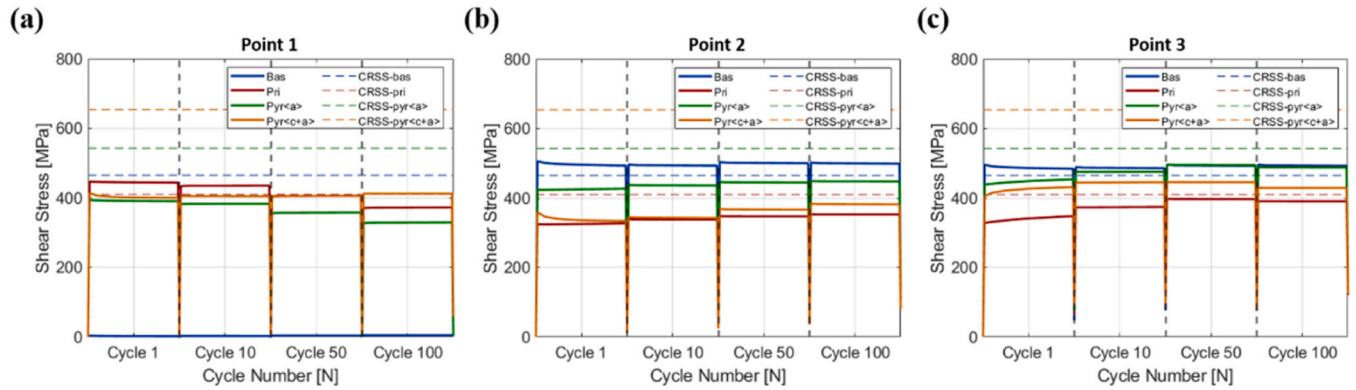

Fig. 12. The shear stress of each slip system at different cycles in S1 at (a) P1, (b) P2 and (c) P3.

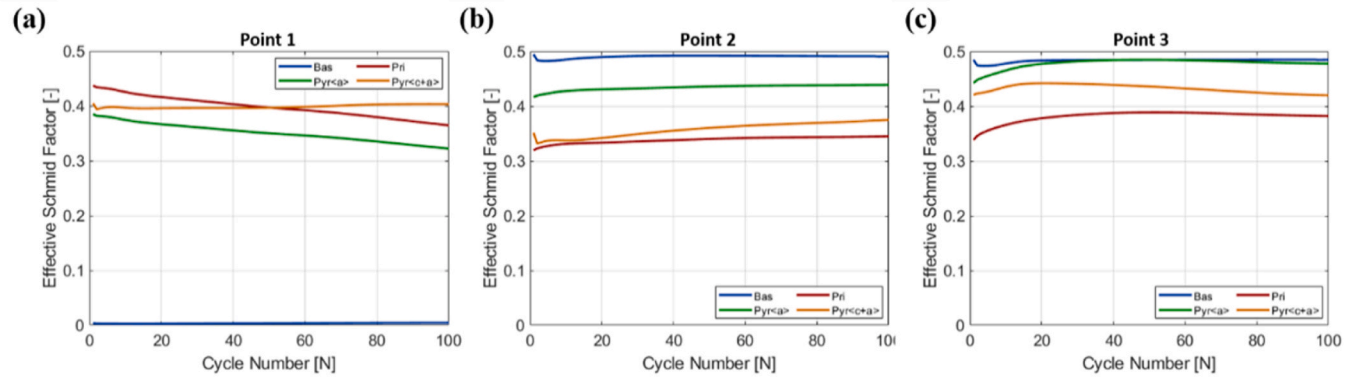

Fig. 13. The ESF of each slip system along with the fatigue cycles at (a) P1, (b) P2 and (c) P3.

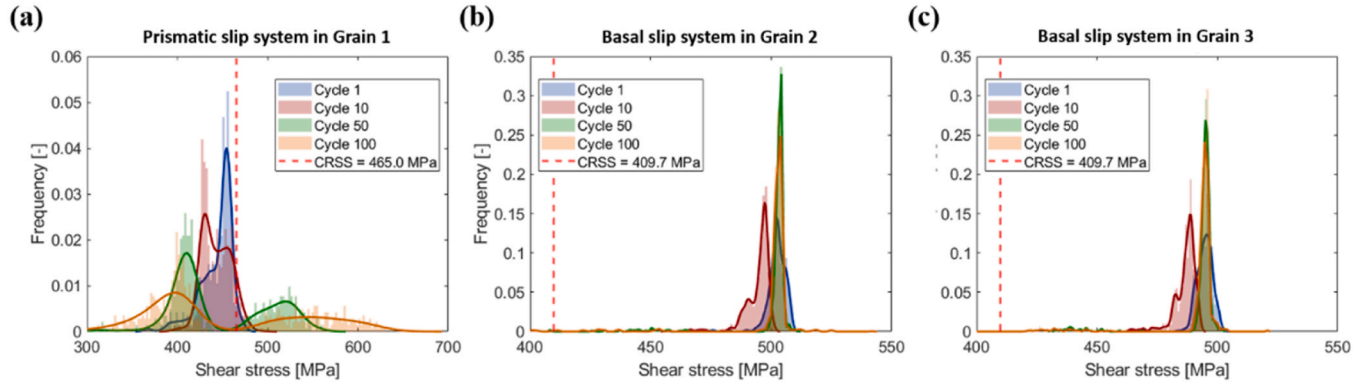

Fig. 14. Shear stress distribution of different slip systems for three grains. (a) Prismatic slip system in G1; (b) basal slip system in G2; (c) basal slip system in G3.

variation can be explained by the redistribution of stress along with the dwell fatigue. For G2 and G3, as shown in Fig. 14 (b) and (c), the basal slip system remains at a consistently high level throughout the dwell-fatigue process, indicating that the basal slip is continuously activated. It can be concluded that the dominant slip systems at these three grains are the basal and prismatic systems, which is consistent with the experimental observations reported by Hu et al. [15] using the HR-DIC technique.

Additionally, when adjacent grains exhibit similar crystallographic orientations, the trend of their stress variation tends to converge as the fatigue cycles increase and dislocation slip accumulates, as indicated in Fig. 10 (c). This phenomenon is likely due to the reduced influence of grain boundaries, as the continuity in lattice orientation facilitates more uniform stress transmission. Conversely, when the misorientation between two neighboring grains is substantial, as observed between G1 and G2 in this study where their orientations are nearly orthogonal, the grain boundary exerts a pronounced barrier effect [20]. This is evidenced by the distinct stress discontinuity at the grain boundary in Fig. 10 (b) and (c), as well as the abrupt change in both the trend and magnitude of stress evolution during the dwell period.

5.2. *Load shedding and slip activity*

To better investigate the load shedding phenomenon throughout the simulation, the maximum stress variation at each point is plotted against the fatigue cycles, as shown in Fig. 15. Notably, the three points exhibited different trends in stress variation over the entire fatigue cycle.

In general, stress redistribution is usually associated with load

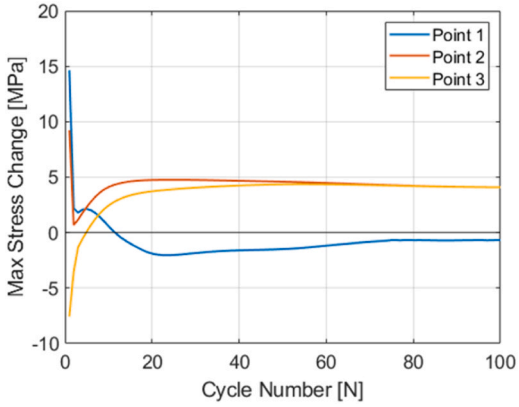

Fig. 15. maximum stress changes along with fatigue cycles in three points in S1.

shedding during the dwell process. Load shedding typically occurs in soft grains as being discussed before. However, it is noteworthy that before the 12th cycle of dwell fatigue, load shedding also occurred in P1, despite it belonging to the grain which was classified as a hard grain based on the SF distribution. In conjunction with the previous discussion on shear stress and ESF of the slip systems, it can be inferred that the load shedding observed in P1 is associated with the activation of the prismatic slip system. As the number of cycles increases and the prismatic slip system can no longer be effectively activated, a stress increase during the dwell period emerges in P1.

P2 exhibits load shedding behavior consistently throughout the entire simulation process. Moreover, at this point, the basal slip system remains continuously activated throughout the whole simulation. In contrast, although P3 shares similarities with P2 in terms of slip activity, it exhibits a noticeable stress increase before the 5th fatigue cycle. This may be attributed to the fact that P2 is located closer to the hard grain compared to P3, resulting in an earlier onset of load shedding in P2.

Based on the trends of slip activity shown in Fig. 14, it is evident that the occurrence of load shedding is synchronized with the activation of prismatic slip in hard grain G1. Therefore, the simulation results suggest that the load shedding phenomenon is most likely primarily governed by prismatic slip, leading to stress reduction due to dislocation cumulation.

5.3. Future approaches

While the proposed methodology offers valuable insights into the dwell fatigue behavior of SLM-processed Ti-6Al-4V beyond the reach of conventional experimental techniques, certain aspects still warrant further refinement.

In this study, the ExaCA tool was employed during the CA process, wherein grain orientations were assigned randomly during the simulation of nucleation. In the actual SLM process, grain nucleation may exhibit preferred orientations [31–33], which are not fully captured in the current setup. The current CPFEM framework focuses primarily on dislocation slip as the dominant deformation mechanism. Other mechanisms such as deformation twinning and the influence of SLM-induced defects are not yet considered, despite their potential relevance to dwell fatigue behavior. Incorporating these effects will be an important focus for future model development.

6. Conclusions

This study proposes a combined numerical approach utilizing CA and CPFE methods to investigate the slip behavior of SLM-processed Ti-6Al-4V material under dwell fatigue, aiming to overcome the time-consuming nature and observational challenges associated with practical experiments. By simulating the SLM process, a more realistic and complex microstructure was generated, and the model parameters were calibrated using tensile test results. Detailed investigations were conducted on grains with different orientations, and the dwell fatigue phenomenon was explained through a quantitative analysis of the slip system behaviors. The main conclusions of this study can be summarized as follows:

(1) ExaCA successfully reconstructed the prior-β grain structure and, by applying the BOR, generated a fully three-dimensional α phase polycrystalline model that reproduces the experimental grain-size distribution and aspect ratio within 5 % deviation. This model can be imported into the CPFE framework for subsequent mechanical analysis.
(2) After embedding the CA-generated microstructure and calibrating the CP model to monotonic tensile data, the combined CA–CPFE approach reproduced the cyclic stress plateau and dwell-fatigue hysteresis characteristic of SLM-processed Ti-6Al-4V, confirming its ability to capture essential micromechanical response.
(3) Systematic evaluation of shear stress and ESF showed that hard grains with comparatively high ESF values in prismatic slip undergo rapid stress redistribution, promoting preferential activation of prismatic slip and thereby initiating load-shedding behavior.
(4) These findings indicate that load shedding originates from local incompatibility in slip resistance caused by orientation heterogeneity. Future work will incorporate temperature-gradient-dependent nucleation, internal defects, and residual stress to achieve even more comprehensive predictions.

CRediT authorship contribution statement

Takayuki Shiraiwa: Writing – review & editing, Supervision, Software, Resources, Methodology, Funding acquisition. **Fabien Briffod:** Writing – review & editing, Software, Methodology. **Masanori Kitamura:** Data curation. **Hanqing Liu:** Writing – original draft, Validation, Software, Methodology, Investigation, Formal analysis, Conceptualization.

Declaration of Competing Interest

The authors declare that they have no known competing financial interests or personal relationships that could have appeared to influence the work reported in this paper.

Acknowledgments

The authors acknowledge the financial support by JSPS KAKENHI Grant Numbers 23H04464, 24H00982, and 21H01648, as well as by the Research Grant from the JFE 21st Century Foundation, the Environmental Research Grant from the Sumitomo Foundation, the Research Grant from the Suzuki Foundation, and the Research Promotion Grant from the Iron and Steel Institute of Japan (ISIJ).

Data availability

The raw/processed data are available from the corresponding author upon reasonable request.

References

[1] T. DebRoy, T. Mukherjee, J.O. Milewski, J.W. Elmer, B. Ribic, J.J. Blecher, et al., Scientific, technological and economic issues in metal printing and their solutions, Nat. Mater. 18 (2019) 1026–1032, https://doi.org/10.1038/s41563-019-0408-2.
[2] T. Kurzynowski, A. Pawlak, I. Smolina, The potential of SLM technology for processing magnesium alloys in aerospace industry, Archiv. Civ. Mech. Eng. 20 (2020), https://doi.org/10.1007/s43452-020-00033-1.

[3] S.P. Yadav, R.S. Pawade, Manufacturing methods induced property variations in Ti6Al4V using High-Speed machining and additive manufacturing (AM), Metals 13 (2023) 287, https://doi.org/10.3390/met13020287.
[4] A.K. Singla, M. Banerjee, A. Sharma, J. Singh, A. Bansal, M.K. Gupta, et al., Selective laser melting of Ti6Al4V alloy: process parameters, defects and post-treatments, J. Manuf. Process. 64 (2021) 161–187, https://doi.org/10.1016/j.jmapro.2021.01.009.
[5] I. Gurrappa, Characterization of titanium alloy Ti-6Al-4V for chemical, marine and industrial applications, Mater. Charact. 51 (2003) 131–139, https://doi.org/10.1016/j.matchar.2003.10.006.
[6] S. Krishnamoorthi, R. Bandyopadhyay, M.D. Sangid, A microstructure-based fatigue model for additively manufactured Ti-6Al-4V, including the role of prior β boundaries, Int. J. Plast. 163 (2023) 103569, https://doi.org/10.1016/j.ijplas.2023.103569.
[7] D. Agius, K.I. Kourousis, C. Wallbrink, A review of the As-Built SLM Ti-6Al-4V mechanical properties towards achieving fatigue resistant designs, Metals 8 (2018) 75, https://doi.org/10.3390/met8010075.
[8] J.-B. Lee, D. Seo, H.Y. Chang, Evaluating corrosion resistance of Additive-Manufactured Ti–6Al–4V using electrochemical critical localized corrosion temperature, Met Mater. Int. 26 (2020) 39–45, https://doi.org/10.1007/s12540-019-00484-z.
[9] Z. Xu, A. Liu, X. Wang, Fatigue performance differences between rolled and selective laser melted Ti6Al4V alloys, Mater. Charact. 189 (2022) 111963, https://doi.org/10.1016/j.matchar.2022.111963.
[10] S.L. Semiatin, V. Seetharaman, I. Weiss, The thermomechanical processing of alpha/beta titanium alloys, JOM 49 (1997) 33–39, https://doi.org/10.1007/BF02914711.
[11] Y. Chong, G. Deng, S. Gao, J. Yi, A. Shibata, N. Tsuji, Yielding nature and Hall-Petch relationships in Ti-6Al-4V alloy with fully equiaxed and bimodal microstructures, Scr. Mater. 172 (2019) 77–82, https://doi.org/10.1016/j.scriptamat.2019.07.015.
[12] A. Azarniya, X.G. Colera, M.J. Mirzaali, S. Sovizi, F. Bartolomeu, M. St Weglowski, k, et al., Additive manufacturing of Ti–6Al–4V parts through laser metal deposition (LMD): process, microstructure, and mechanical properties, J. Alloy. Compd. 804 (2019) 163–191, https://doi.org/10.1016/j.jallcom.2019.04.255.
[13] L. Bhandari, V. Gaur, A study on dwell-fatigue behavior of additively manufactured Ti-alloy, Eng. Fail. Anal. 151 (2023) 107423, https://doi.org/10.1016/j.engfailanal.2023.107423.
[14] A. Townsend, N. Senin, L. Blunt, R.K. Leach, J.S. Taylor, Surface texture metrology for metal additive manufacturing: a review, Precis. Eng. 46 (2016) 34–47, https://doi.org/10.1016/j.precisioneng.2016.06.001.
[15] H. Hu, F. Briffod, W. Yin, T. Shiraiwa, M. Enoki, Quantitative investigation of slip band activities in a bimodal titanium alloy under pure fatigue and dwell-fatigue loadings, Int. J. Fatigue 182 (2024) 108203, https://doi.org/10.1016/j.ijfatigue.2024.108203.
[16] X. Cai, K. Tang, P. Ferro, F. Berto, Coordinated effect of microstructure and defect on fatigue accumulation in dual-phase Ti-6Al-4V: quantitative characterization, Int. J. Fatigue 167 (2023) 107305, https://doi.org/10.1016/j.ijfatigue.2022.107305.
[17] F. Bridier, D.L. McDowell, P. Villechaise, J. Mendez, Crystal plasticity modeling of slip activity in Ti–6Al–4V under high cycle fatigue loading, Int. J. Plast. 25 (2009) 1066–1082, https://doi.org/10.1016/j.ijplas.2008.08.004.
[18] X. Chen, J. Zhang, L. Hu, D. Ji, Investigation on anisotropic behavior of additively manufactured Ti–6Al–4V based on cellular automaton and CPFEM, Met Mater. Int. (2025), https://doi.org/10.1007/s12540-025-01902-1.
[19] V. Hasija, S. Ghosh, M.J. Mills, D.S. Joseph, Deformation and creep modeling in polycrystalline Ti–6Al alloys, Acta Mater. 51 (2003) 4533–4549, https://doi.org/10.1016/S1359-6454(03)00289-1.
[20] Z. Zheng, P. Zhao, M. Zhan, S. Shen, Y. Wang, M.W. Fu, The roles of rise and fall time in load shedding and strain partitioning under the dwell fatigue of titanium alloys with different microstructures, Int. J. Plast. 149 (2022) 103161, https://doi.org/10.1016/j.ijplas.2021.103161.
[21] KITAMURA M. Prediction of process–microstructure relationship in metal additive manufacturing using the cellular automaton method 2025.
[22] M. Rolchigo, S.T. Reeve, B. Stump, G.L. Knapp, J. Coleman, A. Plotkowski, et al., ExaCA: a performance portable exascale cellular automata application for alloy solidification modeling, Comput. Mater. Sci. 214 (2022) 111692, https://doi.org/10.1016/j.commatsci.2022.111692.
[23] W.G. Burgers, On the process of transition of the cubic-body-centered modification into the hexagonal-close-packed modification of zirconium, Physica 1 (1934) 561–586, https://doi.org/10.1016/S0031-8914(34)80244-3.
[24] X. Gao, S. Zhang, L. Wang, K. Yang, P. Wang, H. Chen, Evolution of grain boundary α phase during cooling from β phase field in a α + β titanium alloy, Mater. Lett. 301 (2021) 130318, https://doi.org/10.1016/j.matlet.2021.130318.
[25] N. Miyano, H. Fujiwara, K. Ameyama, G.C. Weatherly, Preferred orientation relationship of intra- and inter-granular precipitates in titanium alloys, Mater. Sci. Eng. A 333 (2002) 85–91, https://doi.org/10.1016/S0921-5093(01)01829-9.
[26] F. Briffod, T. Shiraiwa, M. Enoki, Nucleation and propagation modeling of short fatigue crack in rolled bi-modal Ti–6Al–4V alloy, Mater. Sci. Eng. A 790 (2020) 139710, https://doi.org/10.1016/j.msea.2020.139710.
[27] F. Briffod, T. Shiraiwa, M. Enoki, S. Emura, Effect of macrozones on fatigue crack initiation and propagation mechanisms in a forged ti-6Al-4V alloy under fully-reversed condition, Materialia 22 (2022) 101401, https://doi.org/10.1016/j.mtla.2022.101401.
[28] J.R. Mayeur, D.L. McDowell, A three-dimensional crystal plasticity model for duplex Ti–6Al–4V, Int. J. Plast. 23 (2007) 1457–1485, https://doi.org/10.1016/j.ijplas.2006.11.006.
[29] H. Beladi, Q. Chao, G.S. Rohrer, Variant selection and intervariant crystallographic planes distribution in martensite in a Ti–6Al–4V alloy, Acta Mater. 80 (2014) 478–489, https://doi.org/10.1016/j.actamat.2014.06.064.
[30] S. Hémery, D. Bertheau, F. Hamon, Microtexture effects on fatigue and dwell-fatigue lifetimes of Ti-6Al-4V, Int. J. Fatigue 179 (2024) 108068, https://doi.org/10.1016/j.ijfatigue.2023.108068.
[31] J. Yang, H. Yu, Z. Wang, X. Zeng, Effect of crystallographic orientation on mechanical anisotropy of selective laser melted Ti-6Al-4V alloy, Mater. Charact. 127 (2017) 137–145, https://doi.org/10.1016/j.matchar.2017.01.014.
[32] M. Simonelli, Y.Y. Tse, C. Tuck, Effect of the build orientation on the mechanical properties and fracture modes of SLM Ti–6Al–4V, Mater. Sci. Eng. A 616 (2014) 1–11, https://doi.org/10.1016/j.msea.2014.07.086.
[33] T. Ishimoto, K. Hagihara, K. Hisamoto, T. Nakano, Stability of crystallographic texture in laser powder bed fusion: understanding the competition of crystal growth using a single crystalline seed, Addit. Manuf. 43 (2021) 102004, https://doi.org/10.1016/j.addma.2021.102004.